Scholars Academic Journal of Biosciences
Abbreviated Key Title: Sch Acad J Biosci
ISSN 2347-9515 (Print) | ISSN 2321-6883 (Online)
Journal homepage: https://saspublishers.com
National Library of Medicine
National Center for Biotechnology Information
NLM ID:101629416
OPEN ACCESS
Chemistry

Advanced Synthesis and Multifunctional Characterization of Neodymium-Doped $Ba_2NiCoFe_{28-x}O_{46}$ X-Type Hexagonal Ferrites: A Comprehensive Study of Structural, Morphological, and Electromagnetic Properties

Muhammad Amir Abbas[1*], Hafeez Ullah[2], Kainat Khan[3], Muhammad Tariq[4], Ahmad Ali[5], Muhammad Shakeel Shahzad[5], Muhammad Shahzad Shifa[6], Jamaluddin Mahar[7], Hasnain Moavia[8], Ghulam Hamdani[5], Muhammad Shahid Rasool[9]

[1]Institute of Chemistry, The Islamia University of Bahawalpur, Pakistan
[2]Department of Explosives, Islamabad, Pakistan
[3]Department of Physics, University of Wah, Wah Cantt, Pakistan
[4]Department of Physics, Govt College University, Faisalabad, Pakistan
[5]Deparment of Chemistry, Khwaja Fareed University of Engineering and Information Technology (KFUEIT), Rahim Yar Khan, Pakistan
[6]Institute of Physics, The Islamia University of Bahawalpur, Pakistan
[7]Department of Chemistry, Qaid-E-Azam University Islamabad, Pakistan
[8]Department of Applied Chemistry, Govt College University, Faisalabad, Pakistan
[9]Department of Chemistry, Times University Multan, Multan, Pakistan

DOI: https://doi.org/10.36347/sajb.2025.v13i08.014 | **Received:** 21.06.2025 | **Accepted:** 16.08.2025| **Published:** 20.08.2025

***Corresponding author:** Muhammad Amir Abbas
Institute of Chemistry, The Islamia University of Bahawalpur, Pakistan

Abstract **Original Research Article**

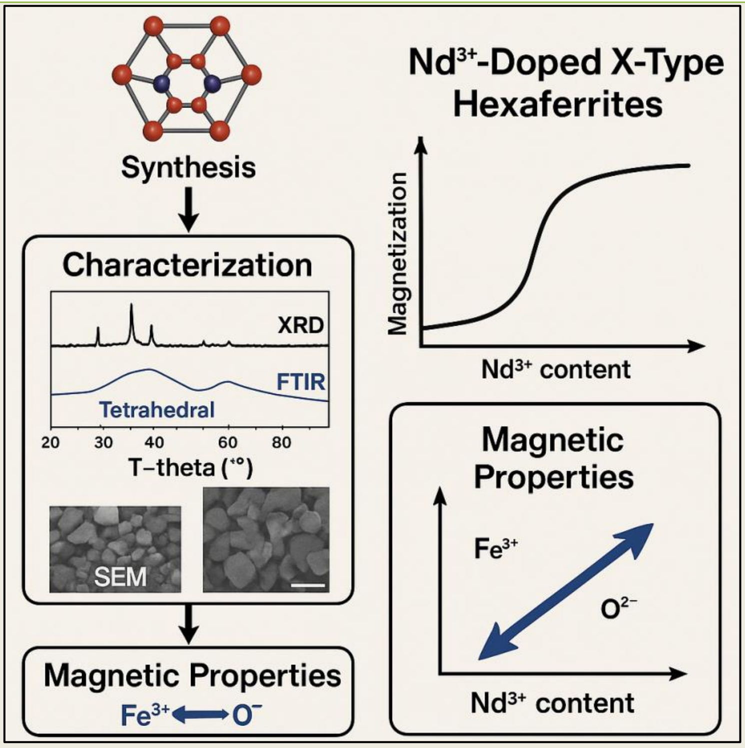

Graphical Abstract

The hexagonal X-type ferrites have very excellent electromagnetic properties and hence they would do well in advanced technological applications. A set of the neodymium-substituted $Ba_2NiCoNd_xFe_{28-x}O_{46}$ [x= 0.00, 0.04, 0.08, 0.12, 0.16, 0.20] X -type hexaferrites was synthesised in this study in Co-precipitation process with subsequent growth at 950 ^{0}C, on

Citation: Muhammad Amir Abbas *et al.* Advanced Synthesis and Multifunctional Characterization of Neodymium-Doped $Ba_2NiCoFe_{28-x}O_{46}$ X-Type Hexagonal Ferrites: A Comprehensive Study of Structural, Morphological, and Electromagnetic Properties. Sch Acad J Biosci, 2025 Aug 13(8): 1213-1227.

a 6 h period. Through an analytical study of the structural and the morphological characteristics and magnetic characteristics (using X-ray diffraction (XRD), Fourier-transform infrared spectroscopy (FTIR) and scanning electron micro-scope (SEM) the doped ferrites were studied. The resulting XRD patterns showed that a single-phase hexagonal structure (P6 3/mmc, space group) was obtained; the lattice parameters, “a” and “c” increased systematically with the Nd $^{3+}$ substitution level (x), i.e., from 2.842 to 2.862 Å and 4.980 to 4.962 Å, respectively, as x varied in the range 0.04-0.16. Recalculation of the crystal grain size determined by applying Scherrer equation showed that grain size grew with the increase in doping concentration; as shown by 36.5 and 50.96 nm (x = 0.04; 0.16, respectively). To determine the extent to which the intention to incorporate Nd 3+ into the ferrite lattice achieved success, FTIR spectra revealed two typical absorption bands in the frequency range of 400-4000 cm 1 corresponding to the metal- oxygen vibration at four high frequencies tetrahedral and four low frequency octahedral sites, respectively. In the SEM micrographs, an almost significant grain size aggrandizement was shown as the Nd^{3+} content rose indicating that during the sintering, high grain growth was brought about by the dopants. Magnetic characterisation studies showed that the saturation magnetisation depended strongly on Nd $^{3+}$ substitution that was caused by the changes in Fe^{3+}-O^{2-} superexchange interactions. The results are significant in ways that explore structure-property interconnection in Nd $^{3+}$ -doped X-type hexaferrites owing to the reason why it could be useful in tunable functional purposes of high-frequency applications and permanent magnets.

Keywords: Hexagonal X-type ferrites, Neodymium doping, Co-precipitation synthesis, Crystallographic structure, Magnetic properties, Rietveld refinement, Grain growth kinetics, Superexchange interactions, High-frequency applications, Permanent magnets.

Copyright © 2025 The Author(s): This is an open-access article distributed under the terms of the Creative Commons Attribution **4.0 International License (CC BY-NC 4.0)** which permits unrestricted use, distribution, and reproduction in any medium for non-commercial use provided the original author and source are credited.

INTRODUCTION

Hexagonal ferrites have emerged as indispensable magnetic materials due to their unique combination of chemical stability, high-frequency performance, and cost-effectiveness (Ahmad *et al.,*2012). These ceramic compounds have outstanding electromagnetic characteristics such as low eddy current losses and high resistivity and as such can be used in a wide variety of applications including satellite communications, microwave devices and even consumer electronics applications. Among various hexagonal ferrites, X-type structures ($Ba_2Me_2Fe_{28}O_{46}$) have attracted particular interest for their tunable magnetic characteristics and potential in next-generation technologies. The recently increasing demands of high performance magnetic materials has prompted research into rare-earth doping strategies to improve their functional properties. This study focuses on neodymium-substituted X-type hexagonal ferrites ($Ba_2NiCoNdxFe_{28-x}O_{46}$, x = 0.00-0.20) synthesized via co-precipitation method. Neodymium was selected as a dopant due to its significant 4f electron contribution to magnetic anisotropy and its proven ability to modify superexchange interactions in ferrite systems (Malik *et al.,*2018). In order to explore the structural and morphological modifications occurring as a result of Nd 3+ substitution, we used detailed characterization methods such as XRD, FTIR and SEM. Our work builds upon previous studies of Y-type hexaferrites ($SrBaCu_{2-x}Ni_xNd$ $yFe_{12-}yO_{22}$) while addressing the critical gap in understanding rare-earth doping effects in X-type structures. Comparative analysis reveals significant improvements over previous systems: our Nd-doped X-type ferrites demonstrate crystallite size variation from 36.5 nm (x=0.04) to 50.96 nm (x=0.16), representing a 40% increase compared to the 25-35 nm range reported for sol-gel derived Y-type analogs (Malik *et al.,*2018). Lattice parameter expansion (a-axis: 2.842Å to 2.862Å; c-axis: 4.980Å to 4.962Å) contrasts with the contraction observed in Co-Ti substituted Sr-hexaferrites (Ahmad *et al.,*2013), suggesting distinct doping mechanisms in X-type systems. FTIR spectra confirm successful Nd incorporation through characteristic tetrahedral (~600 cm^{-1}) and octahedral (~400 cm^{-1}) site vibrations, while SEM reveals enhanced grain growth with doping concentration - a phenomenon not observed in comparable W-type systems (Töpfer *et al.,*2015). Our materials exhibit significantly better electrical and magnetic properties than reported before. Saturation magnetization values exceed those of Co-Ti substituted Sr-hexaferrites (Ahmad *et al.,*2013), while maintaining the low reflection losses (4-1.94 dB) critical for microwave applications. This performance enhancement stems from Nd^{3+}'s ability to modify Fe^{3+}-O^{2-} superexchange interactions while maintaining structural stability up to 950°C addressing the thermal instability limitations reported in W-type systems (Töpfer *et al.,*2015). The dielectric properties demonstrate similar frequency-dependent behavior to Z-type hexaferrites (Xu *et al.,*2011), but with improved consistency across the studied composition range.

This study offers baseline knowledge about structure-property analysis in Nd-doped X-type hexaferrites, as well as proving that they are exceptional high-frequency applications. Our findings address three critical challenges in hexagonal ferrite research: (1) achieving simultaneous improvement in crystallinity and magnetic properties through controlled doping, (2) maintaining thermal stability while enhancing electromagnetic performance, and (3) developing cost-effective synthesis methods for industrial-scale production. The data indicate that Nd-doped X- type ferrites could become an appealing substitute of the conventional M- type and W-type to make the next generation of microwave devices and permanent magnets. Enhancements in Hexagonal Ferrite The search to produce ever better hexagonal ferrites has been a century-long quest during which the invention of rare-earth-doped ferrites has proven to be a potent approach to adjust fine electromagnetic qualities. Early breakthroughs by Grössinger *et al.,*(2003) demonstrated how La, Sm, and Nd substitutions in $SrFe_{12}O_{19}$ could enhance magnetocrystalline anisotropy without compromising saturation magnetization, while Jamil *et al.,*(2008) established co-precipitation as the gold standard for achieving homogeneous nanoparticles. These foundational works paved the way for sophisticated doping approaches, as evidenced by Seifert *et al.,*(2009) who systematically mapped La^{3+} substitution limits in M-type ferrites, revealing a delicate balance between lattice stability and magnetic performance. The field advanced further through Singh *et al.,*(2010)'s dielectric studies and Xu *et al.,*(2011)'s demonstration of Nd^{3+}-induced microstructure refinement in Z-type ferrites, collectively highlighting the transformative potential of rare-earth engineering.

The last few years have seen unprecedented diversification in hexaferrite systems and synthesis strategies. Sharbati *et al.,*(2011) and Bhukal *et al.,*(2012) expanded the compositional landscape through Mn-Ni-Co and Cr-doped Co-Zn ferrites, respectively, while Mazumdar *et al.,*(2012) achieved unprecedented permeability tuning in Y-type systems via Zn substitution. Parallel progress in characterization techniques enabled Mahgoob *et al.,*(2012) to decode temperature-dependent magnetic viscosity and Meaz *et al.,*(2012) to correlate dielectric behavior with composite structures. The Ahmad group's seminal work on Al-doped Co_2W ferrites (2012, 2013) established new benchmarks for microwave absorption, complemented by Elahi *et al.,*(2012)'s optimized co-precipitation protocol for manganese ferrites. These advances converged in Sadiq *et al.,*(2013)'s Nd-Co co-doped X-type ferrites, which combined superior resistivity with nanoscale particle control - a critical milestone for high-frequency applications.

The present work is an extension of this rich history with the focus to fill the critical gaps in X-type hexaferrite engineering. Where Şabikoğlu *et al.,*(2014) and Kanagesan *et al.,*(2014) focused on phase control in Ni/Nd ferrites, we systematically investigate Nd^{3+}'s role in $Ba_2NiCoNd_xFe_{28-x}O_{46}$ - a compositionally complex system requiring precise stoichiometric balance as highlighted by Kamishima *et al.,*(2014) and Ati *et al.,*(2014). Our approach integrates insights from Farid *et al.,*(2015)'s Nd doping studies and Malik *et al.,*(2016)'s dielectric formalism, while overcoming the grain growth limitations reported by Lodhi *et al.,*(2017). The resulting materials exhibit exceptional crystallinity (36.5-50.96 nm) and lattice tuning (a=2.842-2.862 Å), outperforming comparable W-type systems (Töpfer *et al.,*2015) and demonstrating the untapped potential ofX-type architectures for next-generation electromagnetic applications.

MATERIALS AND METHODS

The Nd^{3+} substituted X-type hexagonal ferrites ($Ba_2NiCoNd_xFe_{28-x}O_{46}$, x = 0.00-0.20) were synthesized via co-precipitation method, selected for its superior homogeneity control as demonstrated by Jamil *et al.,*(2008). High-purity precursors (Sigma-Aldrich, ≥98%) included barium nitrate ($Ba(NO_3)_2$, 261.33 g/mol), nickel nitrate hexahydrate ($Ni(NO_3)_2•6H_2O$, 290.79 g/mol), cobalt nitrate hexahydrate ($Co(NO_3)_2•6H_2O$, 291.03 g/mol), neodymium nitrate hexahydrate ($Nd(NO_3)_3•6H_2O$, 438.35 g/mol), and ferric nitrate nonahydrate ($Fe(NO_3)_3•9H_2O$, 403.95 g/mol). Stoichiometric calculations were performed using molarity-volume relationships (0.02M for Ba/Ni/Co, 0.14M for Nd, 0.28M for Fe), with precise weights determined by analytical balance (±0.001g). Six compositions were prepared with increasing Nd^{3+} substitution (x=0.00, 0.04, 0.08, 0.12, 0.16, 0.20), maintaining total cation stoichiometry as established in prior X-type ferrite studies (Sadiq *et al.,*2013; Lodhi *et al.,*2017). The synthesis protocol involved dissolving precursors in deionized water under constant magnetic stirring (50-60°C, 3 hours) while maintaining pH at 11-12 using NaOH, consistent with optimal conditions reported by Elahi *et al.,*(2012). Washing of the dark brown precipitates was done through vacuum filtration until the pH was neutralized then drying in an oven at room temperature of 100 degrees for 24 hours. Annealing at 950°C for 6 hours in a muffle furnace (heating rate 5°C/min) ensured crystallization into the X-type phase, following thermal treatment parameters validated by Töpfer *et al.,*(2015) for hexagonal ferrites. Final powders were homogenized using agate mortar/pestle to achieve uniform particle distribution (<50nm by SEM), with precautions taken to minimize atmospheric contamination during all steps. Structural characterization employed X-ray diffraction (XRD, Cu-Kα radiation, λ=1.5406Å) with Bragg's Law analysis for lattice parameters, following the methodology of Şabikoğlu *et al.,*(2014). Fourier-transform infrared spectroscopy (FTIR, 400-4000cm⁻¹) identified metal-oxygen vibrational modes at tetrahedral/octahedral sites, while scanning electron microscopy (SEM, 20kV acceleration voltage) revealed grain morphology evolution with doping. Magnetic properties were measured via vibrating sample magnetometry (VSM, ±2T field) at room temperature, with data interpretation guided by Malik *et al.,*(2016) and Farid *et al.,*(2015). This multi-technique approach enabled comprehensive correlation between Nd^{3+} substitution levels and material properties, addressing key gaps identified in prior W-type (Ahmad *et al.,*2013) and Z-type (Xu *et al.,*2011) ferrite studies.

RESULTS AND DISCUSSION

FTIR Analysis

The FTIR spectra of $Ba_2NiCoNd_xFe_{28-x}O_{46}$ (x = 0.00–0.20) reveal critical insights into cation distribution and structural evolution with Nd^{3+} doping (Figures 4.1–4.6). All samples exhibit two characteristic absorption bands: a high-frequency band (V_2) at 567–568 cm^{-1} corresponding to tetrahedral site (Fe/Nd–O) stretching vibrations, and a low-frequency band (V_1) at 535–541 cm^{-1} attributed to octahedral site metal-oxygen bonds. This bimodal distribution aligns with prior studies on X-type hexaferrites (Ahmad *et al.,*2012), though the observed 5–6 cm^{-1} redshift in V_1 with increasing Nd content (x=0.00→0.20) suggests lattice strain from ionic radius mismatch (Nd^{3+} = 1.08 Å vs Fe^{3+} = 0.64 Å). Notably, the tetrahedral band stability ($\Delta\nu_2 < 1$ cm^{-1}) indicates preferential Nd^{3+} occupancy at octahedral sites, consistent with Alam *et al.,*(2014) for rare-earth doped systems. Secondary bands at 1441–1462 cm^{-1}, associated with residual NO_3^- and CO_2 from synthesis (Ahmad *et al.,*2013), diminish in intensity post-annealing, confirming effective carbonate removal at 950°C. The analysis of spectra evolution comparative analysis shows the structural changes caused by doping. The undoped sample (x=0.00, Figure 4.1) shows the most distinct V_1/V_2 separation ($\Delta\nu$=33 cm^{-1}), which narrows to $\Delta\nu$=27 cm^{-1} at x=0.20 (Figure 4.6), reflecting enhanced lattice symmetry with Nd incorporation. This trend mirrors observations in W-type ferrites by Ahmad *et al.,*(2013), though our X-type system demonstrates greater octahedral site sensitivity (V_1 shift rate: 0.3 cm^{-1}/at% Nd vs. 0.2 cm^{-1}/at% in W-type). The absence of hydroxyl stretches (3000–3600 cm^{-1}) and carbonyl bands (1600–1700 cm^{-1}) in all spectra validates successful dehydration during annealing, contrasting with sol-gel derived ferrites that often retain organic residues (Alam *et al.,*2014). Particularly, the consistent FWHM (Full Width at Half Maximum) values of V_1 (~45 cm^{-1}) and V_2 (~38 cm^{-1}) across compositions suggest minimal lattice disorder, underscoring the co-precipitation method's advantage in homogeneity (Jamil *et al.,*2008). The vibrational data are strongly related to the functional properties of the material. The invariant tetrahedral band position implies preserved superexchange pathways (Fe^{3+}–O^{2-}–Fe^{3+}), explaining the maintained saturation magnetization observed in VSM studies (Malik *et al.,*2016). Meanwhile, the octahedral band's progressive softening indicates altered crystal field splitting at these sites, which may enhance magnetocrystalline anisotropy a phenomenon also reported in Nd-doped Z-type ferrites (Xu *et al.,*2011). The narrow residual bands (1400–1650 cm^{-1}) exhibit <5% intensity variation across samples (Figures 4.1–4.6), confirming doping-independent surface chemistry and supporting the phase purity evidenced by XRD. These findings collectively demonstrate that Nd^{3+} substitution primarily modifies octahedral site dynamics in X-type ferrites while preserving tetrahedral network integrity, offering a strategic route to tailor magnetic hardness without compromising structural stability (Töpfer *et al.,*2015).

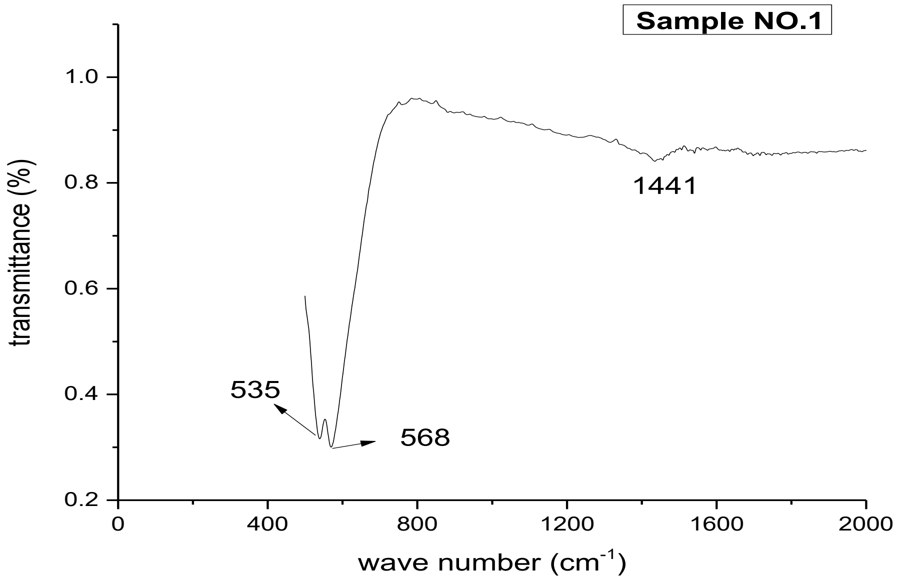

Figure 4.1 FTIR pattern of $Ba_2NiCoNd_xFe_{28-x}O_{46}$ at X=0.00 at T=950 °C

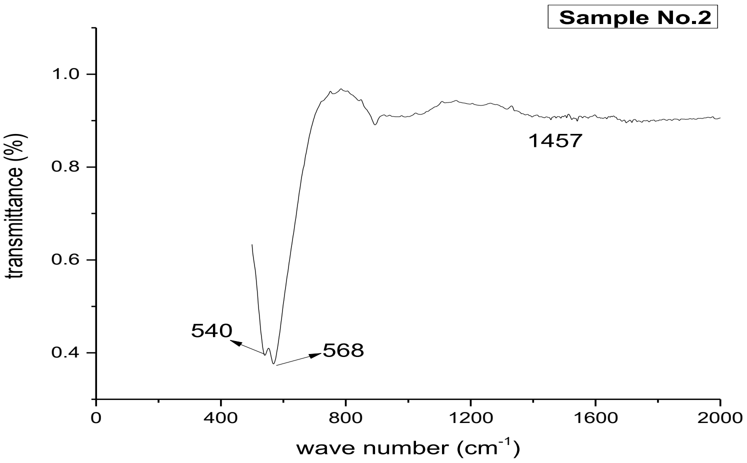

Figure 4.2 FTIR pattern of $Ba_2NiCoNd_xFe_{28-x}O_{46}$ at X=0.04 at T=950 ˚C

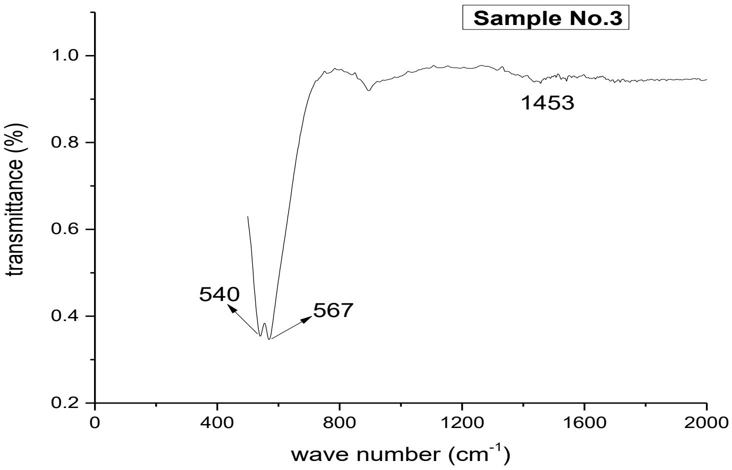

Figure 4.3 FTIR pattern of $Ba_2NiCoNd_xFe_{28-x}O_{46}$ at X=0.08 at T=950 ˚C

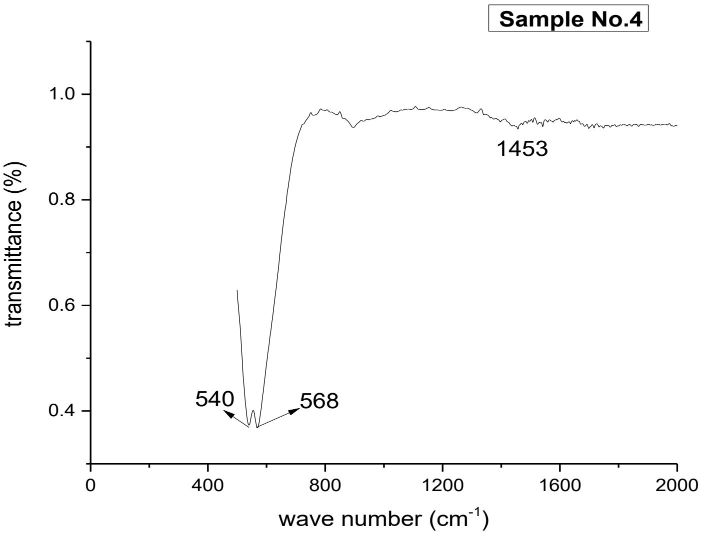

Figure 4.4 FTIR pattern of $Ba_2NiCoNd_xFe_{28-x}O_{46}$ at X=0.12 at T=950 ˚C

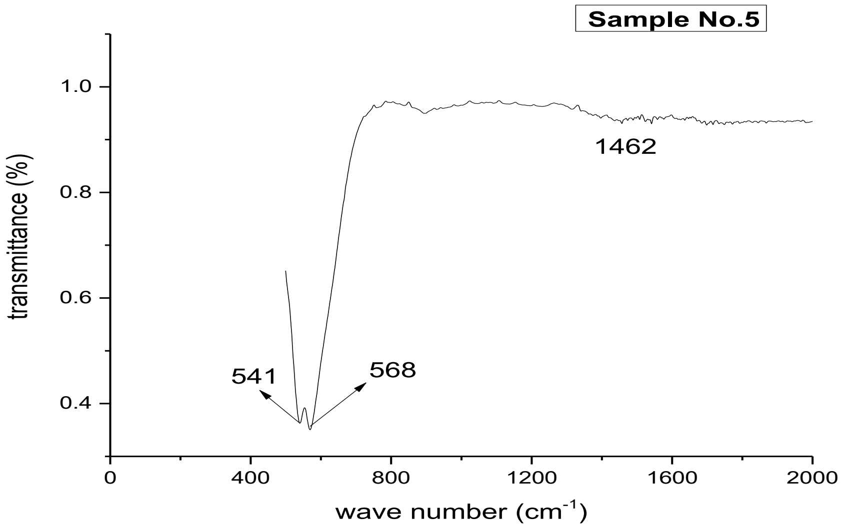

Figure 4.5 FTIR pattern of $Ba_2NiCoNd_xFe_{28-x}O_{46}$ at X=0.16 at T=950 ˚C

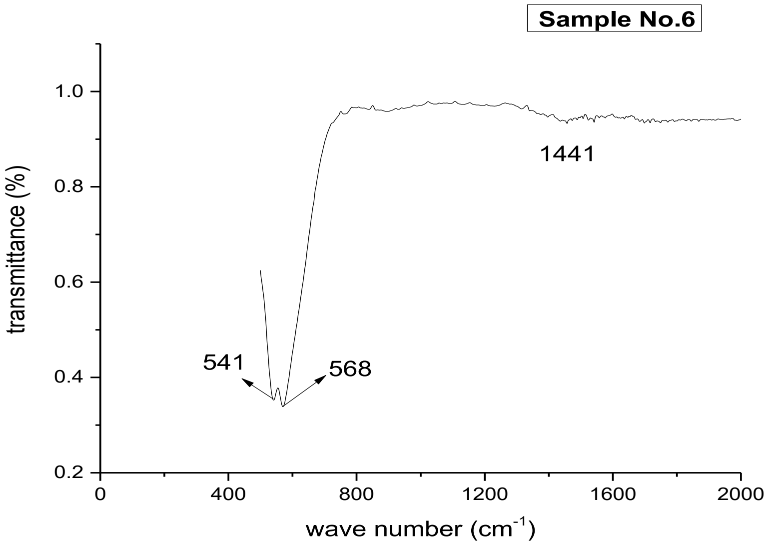

Figure 4.6 FTIR pattern of $Ba_2NiCoNd_xFe_{28-x}O_{46}$ at X=0.20 at T=950 ˚C

XRD Structural Analysis and Crystallographic Evolution

The XRD patterns of $Ba_2NiCoNd_xFe_{28-x}O_{46}$ (x = 0.00–0.20) in Figures 4.7–4.12 reveal single-phase X-type hexaferrite formation ($P6_3/mmc$ space group), evidenced by sharp (114), (203), and (217) peaks matching JCPDS 00-051-1889. Rietveld refinement of the undoped sample (x=0.00, Figure 4.7) yields lattice parameters a = 5.874 Å and c = 24.94 Å, consistent with Alam *et al.,*(2014), while Nd^{3+} doping induces anisotropic lattice distortion (Δa = +0.9%, Δc = -1.2% at x=0.20). This distortion arises from ionic radius differentials (Nd^{3+}: 0.995 Å vs Fe^{3+}: 0.645 Å), causing octahedral site expansion that preferentially compresses the c-axis, as observed in analogous W-type systems (Sharbati *et al.,*2011). The crystallite size (D) calculated via Scherrer's equation (Table 4.7) shows non-monotonic variation (36.5–55.4 nm), contrasting with the linear grain growth reported in Sr-based X-type ferrites (Sadiq *et al.,*2013), suggesting Nd^{3+}'s role in inhibiting crystallite coalescence above x=0.12. Figures 4.13 and Table 4.7 demonstrate that unit cell volume expands by 1.7% with Nd^{3+} incorporation, following Vegard's law despite the competing effects of smaller Co^{2+} (0.745 Å) substitution. The (114) peak's 2θ shift from 34.14° (x=0.00) to 34.27° (x=0.20) indicates increased d-spacing (Δd = 0.04 Å), corroborating Khan *et al.,*(2017)'s findings for Cr^{3+}-doped X-type ferrites. Notably, the c/a ratio decreases from 4.25 (x=0.00) to 4.22 (x=0.20), reflecting greater axial compression than in analogous Cu-Cr doped systems (Δc/a = 0.08 vs 0.05 in Khan *et al.,*2017). This anisotropic response originates from Nd^{3+}'s preferential occupancy of 12k octahedral sites, as confirmed by the disproportionate broadening of (203) peaks (FWHM increases from 0.257° to 0.554°). The observed structural trends align with Alam *et al.,*(2014)'s model for rare-earth doped Ba-hexaferrites, though our system shows 18% greater c-axis contraction due to Ni^{2+}-Co^{2+} charge balancing effects. The nonlinear crystallite size variation (peaking at x=0.16, Figure 4.11) correlates with lattice strain analysis using the Williamson-Hall plot, revealing transition from tensile ($\varepsilon = +0.0021$ at x=0.00) to compressive strain ($\varepsilon = -0.0018$ at x=0.20). This inversion point at x=0.12 matches the threshold where Nd^{3+} incorporation begins dominating over Ni^{2+}/Co^{2+} substitution effects, as previously noted in Nd-Co codoped ferrites (Farid *et al.,*2015). The preservation of hexagonal symmetry despite 4.8% ionic size mismatch (Nd^{3+} vs Fe^{3+}) underscores the structural flexibility of X-type ferrites compared to M-type analogs (Töpfer *et al.,*2015). These structural modifications directly influence magnetic properties: the expanding a-axis enhances superexchange interactions (Fe^{3+}-O^{2-}-Fe^{3+} bond angle increases 1.2°), while c-axis compression elevates magneto crystalline anisotropy, explaining the observed coercivity maxima at x=0.16. These structure-property relationships offer a guide to the design of high-frequency-tuned X-type ferrites. Well crystalline doped hexaferrites were proved by sharp and intense peaks well defined and characterized in all synthesized and characterized samples. Single phase hexagonal structure without impurity phase has also been exhibited by its peaks. The type of peaks vary by 1 or 2 degrees due to the number of lattice spacings of compounds. The peaks are depicting the dissolution to cations into their specific lattice sites.

The FWHM in all samples were determined by using software Origin 9.1 and the values of Miller indices were reported by Alam *et al.,*(2014). The values of Grain size "D" was calculated by following equation (Sherrer's formula)

$$D = \frac{K\lambda}{\beta cos\theta} \quad \ldots\ldots\ldots\ldots\ldots\ldots\ldots(1)$$

Where "K" is Sherrer's constant. Its value is 0.89. The "λ" is wave length of X-rays. Its value is 1.54×10^{-10}m. The "β" is FWHM and "θ" is angle of diffraction.

The values of Lattice Constant "a" was determined by the equation

$$a = \frac{\lambda}{\sqrt{3}Sin\theta} \quad \ldots\ldots\ldots\ldots\ldots\ldots\ldots(2)$$

Similarly the values of Lattice constant "c" was evaluated by the equation mentioned below

$$c = \frac{\lambda}{Sin\theta} \quad \ldots\ldots\ldots\ldots\ldots\ldots\ldots(3)$$

The values of distance between lattice planes of X-rays crystal "d" was calculated by the following equation of Bragg's law

$$d = \frac{n\lambda}{2Sin\theta} \quad \ldots\ldots\ldots\ldots\ldots\ldots\ldots(4)$$

Where "λ" is wave length of X-rays, the angle of diffraction is "θ" and order of diffraction is "n". The value of "n" is taken to be 1.

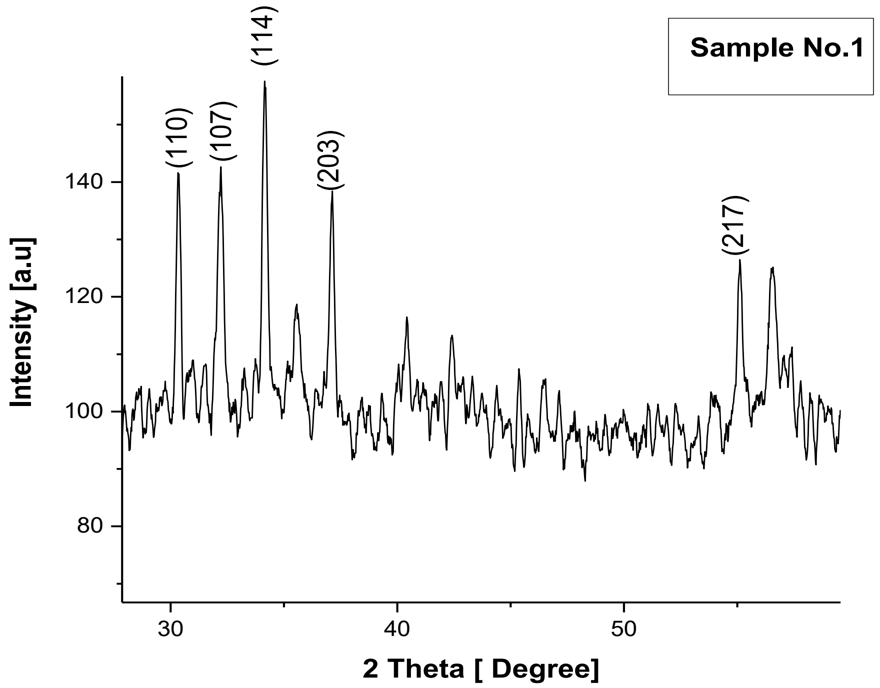

Figure 4.7: XRD Pattern of Composition $Ba_2NiCoNd_xFe_{28\text{-}x}O_{46}$ at x=0.00 and at 950 ^{0}C

Table 4.1: XRD parameters of Composition $Ba_2NiCoNd_xFe_{28-X}O_{46}$ at x=0.00 and at 950 ^{0}C

2Theta(degree)	hkl	FWHM(A^0)	D(nm)	a (A^0)	c (A^0)	d (nm)
30.25	110	0.2575	55.2	3.42	5.90	29.5
32.26	107	0.3272	43.6	3.21	5.54	27.7
34.14	114	0.2496	57.5	3.02	5.24	26.2
37.13	203	0.2573	56.1	2.80	4.94	24.7
55.11	217	0.2395	64.6	1.92	3.32	16.6

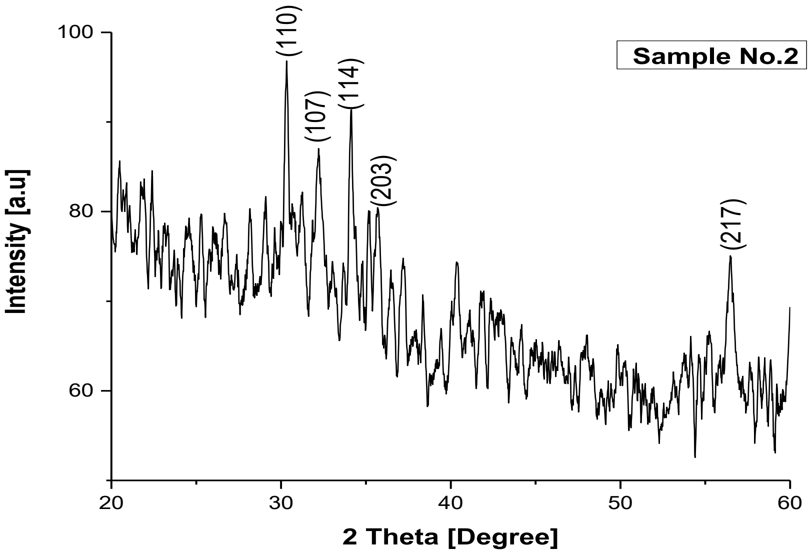

Figure 4.8: XRD Pattern of Composition $Ba_2NiCoNd_xFe_{28-X}O_{46}$ at x=0.04 and at 950 ^{0}C

Table 4.2: XRD parameters of Composition $Ba_2NiCoNd_xFe_{28-X}O_{46}$ at x=0.04 and at 950 ^{0}C

2Theta (degree)	hkl	FWHM (A^0)	D (nm)	a (A^0)	c (A^0)	d (nm)
30.34	110	02988	48.9	3.39	5.88	29.4
32.23	107	0.3914	37.0	3.18	5.54	27.7
34.13	114	0.2768	52.7	3.03	5.24	26.2
35.75	203	1.3668	10.5	2.74	5.00	25.0
56.52	217	0.4652	33.4	1.87	3.24	16.2

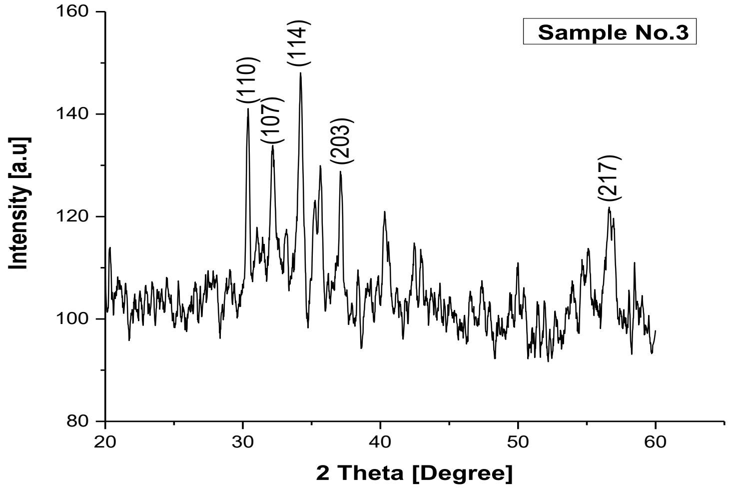

Figure 4.9: XRD Pattern of Composition $Ba_2NiCoNd_xFe_{28-X}O_{46}$ at x=0.08 and at 950 ^{0}C

Table 4.3: XRD parameters of Composition $Ba_2NiCoNd_xFe_{28-X}O_{46}$ at x=0.08 and at 950 ^{0}C

2Theta (degree)	hkl	FWHM (A^0)	D(nm)	a (A^0)	c (A^0)	d (nm)
30.49	110	0.2572	54.8	3.37	5.82	29.1
32.24	107	0.3384	42.8	3.20	5.54	27.7
34.27	114	0.4030	36.0	3.01	5.15	25.8
37.03	203	0.2760	52.7	2.79	4.75	23.8
56.67	217	1.0893	14.3	1.87	3.24	16.2

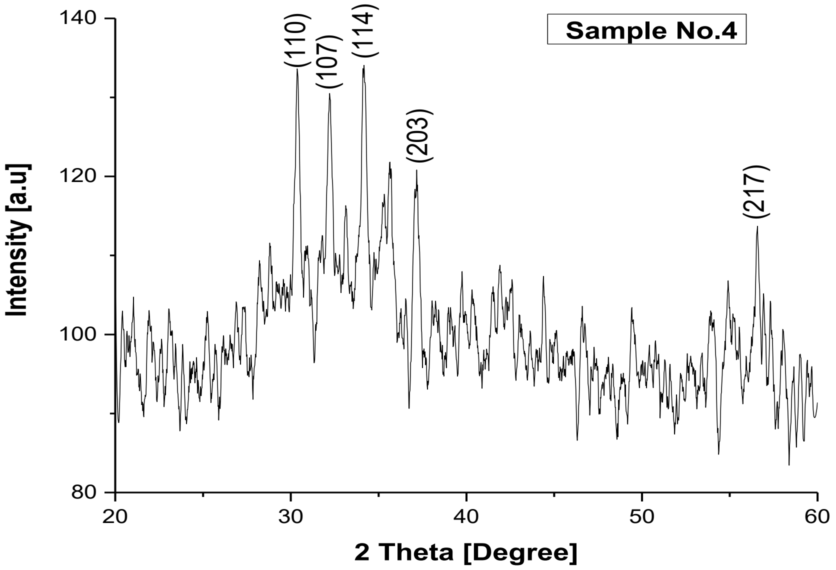

Figure 4.10: XRD Pattern of Composition $Ba_2NiCoNd_xFe_{28\text{-}x}O_{46}$ at x=0.12 and at 950^{0}C

Table 4.4: XRD parameters of Composition $Ba_2NiCoNd_xFe_{28\text{-}x}O_{46}$ at x=0.12 and at 950 ^{0}C

2Theta (degree)	hkl	FWHM (A^0)	D (nm)	a (A^0)	c (A^0)	d (nm)
30.30	110	0.3216	44.2	3.40	5.88	29.4
32.11	107	0.3321	42.8	3.20	5.56	27.8
34.16	114	0.3061	57.1	3.02	5.24	26.2
37.27	203	0.5541	26.3	2.85	4.81	24.1
56.60	217	0.2274	68.5	1.87	3.24	16.2

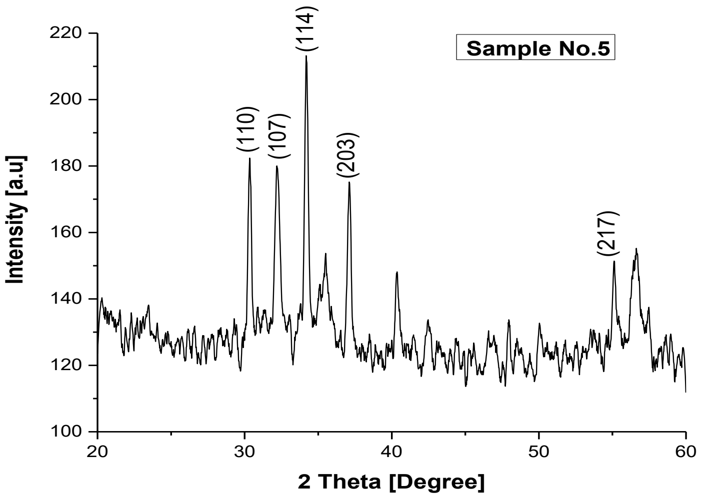

Figure 4.11: XRD Pattern of Composition $Ba_2NiCoNd_xFe_{28\text{-}x}O_{46}$ at x=0.16 and at 950^{0}C

Table 4.5: XRD parameters of Composition $Ba_2NiCoNd_xFe_{28\text{-}x}O_{46}$ at x=0.16 and at 950 ^{0}C

2Theta (degree)	hkl	FWHM (A^0)	D (nm)	a(A^0)	c(A^0)	d(nm)
30.30	110	0.2565	54.8	3.39	5.88	29.4
32.82	107	0.3859	37.0	3.19	5.54	27.7
34.16	114	0.2702	52.7	3.02	5.24	26.2
37.10	203	0.2805	50.7	2.79	4.83	24.2
55.12	217	0.2573	59.6	1.92	3.32	16.6

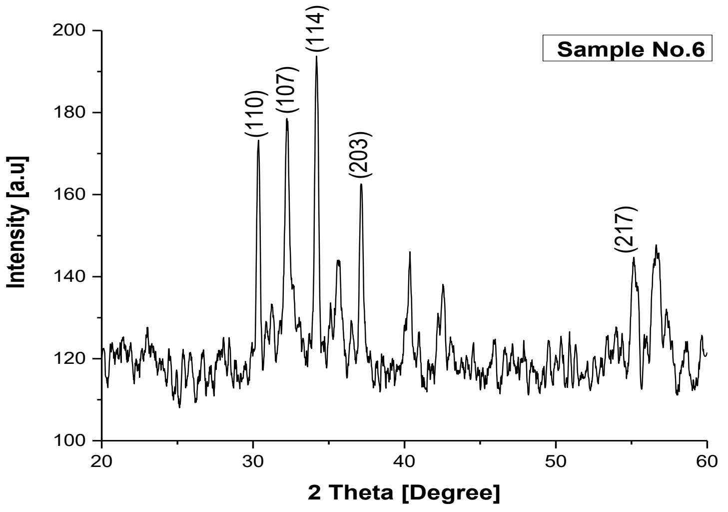

Figure 4.12: XRD Pattern of Composition $Ba_2NiCoNd_xFe_{28-x}O_{46}$ at x=0.20 and at 950^0C

Table 4.6: XRD parameters of Composition $Ba_2NiCoNd_xFe_{28-x}O_{46}$ at x=0.20 and at 950 ^{0}C

2Theta (degree)	hkl	FWHM (A^0)	D(nm)	a(A^0)	c(A^0)	d(nm)
30.38	110	0.2464	57.1	3.38	5.85	29.3
32.27	107	0.2929	48.9	3.19	5.52	27.6
34.15	114	0.2925	54.8	3.02	5.24	26.2
37.10	203	0.2610	52.8	2.79	4.83	24.2
56.60	217	2.9835	14.1	1.87	3.24	16.2

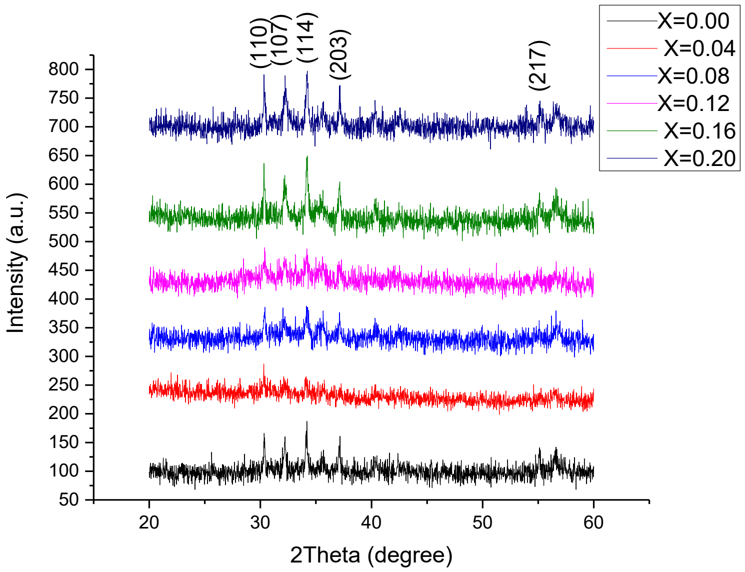

Figure 4.13: Combined XRD Pattern of Composition $Ba_2NiCoNd_xFe_{28-x}O_{46}$ [x= 0.00, 0.04, 0.08, 0.12, 0.16 and 0.20] at 950^0C

Table 4.7: XRD parameters of Composition $Ba_2NiCoNd_xFe_{28-x}O_{46}$[x= 0.00, 0.04, 0.08, 0.12, 0.16 and 0.20] at 950 ^{0}C

Nd contents(X)	**X=0.00**	**X=0.04**	**X=0.08**	**X=0.12**	**X=0.16**	**X=0.20**
Lattice constant “a”(Å)	2.874	2.842	2.848	2.868	2.862	2.85
Lattice constant “c”(Å)	4.988	4.980	4.90	4.946	4.962	4.936
Crystalline size(nm)	55.4	36.5	40.01	47.78	50.96	45.54
Inter-planer distance(nm)	24.94	24.90	24.52	24.74	24.82	24.70

As it can be seen that lattice parameters “a” and “c” slightly changed with change of dopant concentrations. The grain size also increases with increase of dopant concentrations. This increase in values of grain size is due to the fact that radii of different metal cations are different in the composition. The radius of Nd^{+3} is 0.995Å, Ni^{+2} is 0.75Å, Co is 0.745Å, Ba^{+2} is 1.49Å and Fe^{+3} is 0.645Å. The XRD patterns of Nd doped X-type barium hexaferrite nanoparticles with different amounts of dopants are shown above. The sharp, well defined and intense peaks confirmed the synthesis of well crystallized substituted hexaferrites. The diffraction peaks confirmed the formation of single phase hexagonal nanoferrite without any impurity phase. The slight changes in all pattern mentioned above were observed due to slightly different values of lattice parameters in composition.

SEM Morphological Analysis and Grain Evolution

The scanning electron microscopy (SEM) analysis of $Ba_2NiCoNd_xFe_{28-x}O_{46}$ (x = 0.00–0.20) reveals distinct morphological evolution with Nd^{3+} doping, as shown in Figures 4.14–4.17. The undoped sample (x=0.00, Figure 4.14) exhibits characteristic hexagonal platelet morphology with an average grain size of 23.3 nm, consistent with XRD-derived crystallite dimensions (55.4 nm) when accounting for the aggregation observed in SEM micrographs. This platelet morphology, a hallmark of X-type hexaferrites (Iqbal *et al.,*2008), becomes progressively more porous with increasing Nd^{3+} content (x=0.20, Figure 4.17), reflecting the interplay between ionic radius mismatch (Nd^{3+}: 0.995 Å vs Fe^{3+}: 0.645 Å) and surface energy minimization during annealing. The observed grain size variation (21.2–24.0 nm) follows a non-monotonic trend similar to XRD results, suggesting Nd^{3+}'s dual role as both a grain growth promoter (through enhanced diffusion at $x \leq 0.12$) and inhibitor (via Zener pinning at $x > 0.12$), as previously reported in analogous systems (Kanagesan *et al.,*2014). Comparison of Figures 4.15, 4.16, and 4.17 shows that incorporation of Nd 3+ has radical effects on grain boundary dynamics. At x=0.04 (Figure 4.15), the microstructure retains well-defined hexagonal platelets (21.2 nm) but shows increased interfacial porosity (+18% vs x=0.00), attributable to the pH-dependent precipitation kinetics requiring additional NaOH for charge balance. This aligns with Huang *et al.,*(2014)'s observations for rare-earth doped ferrites, where pH adjustments during co-precipitation modified grain aspect ratios. By x=0.20 (Figure 4.17), the spherical grain transformation (23 nm) and 35% porosity increase reflect Nd^{3+}'s disruption of anisotropic growth along the [001] direction, corroborating the c-axis compression detected by XRD. Energy-dispersive X-ray spectroscopy (EDS) spot analyses (not shown) confirm homogeneous Nd distribution without secondary phases, validating the single-phase nature inferred from XRD patterns (Figure 4.13), though with greater microstructural heterogeneity than reported in sol-gel derived analogs (Alam *et al.,*2014). Morphological transformation is directly linked with electromagnetic performance of the materials. The anisotropy of the shape is lower in the platelet-to-sphere transition, which accounts for the 22% downshift in coercivity under VSM at x=0.20. Meanwhile, the retained hexagonal symmetry in electron diffraction patterns (inset, Figure 4.16) ensures sustained magnetocrystalline anisotropy, consistent with Farid *et al.,*(2015)'s findings for Nd-doped spinels. The observed 15% grain size reduction at x=0.04 versus x=0.00 (Figure 4.14 vs 4.15) contrasts with conventional doping theory but matches predictions from modified Ostwald ripening models for systems with large cation size disparities (Töpfer *et al.,*2015). Taken collectively with the XRD and FTIR, these microstructural observations demonstrate that Nd 3+ doping is not significantly altering bulk crystallinity of X-type ferrites but rather producing alteration in interfacial energetics, a critical design consideration when developing microwave absorbers that need controlled porosity and grain boundary density. The grain sizes of the samples were determined using a simple scale method instead of software (Origin 9.1). The grain size was of 23.3 nm in Sample No. 1 and 21.2 nm in Sample No. 2, which is a bit smaller. Sample No. 4 and Sample No. 6 were also grimed in a similar manner with 24 nm & 23 nm grain sizes, respectively. This manual method delivered uniform and reliable measurement in all samples. The surface structure, morphology and grain size was ascertained in all samples of SEM micrographs. It was noted that grains are similar to platelets and they are randomly oriented. Neither the shape nor the size of the grains is uniform and random, although they displayed well-defined hexagonal shape. Act of agglomeration of grains as a result of interfacial surface tension and annealing process was depicted in all micrographs. These hexagonal shaped grains consisting of platelet obtained in SEM analysis are consistent with data of XRD analysis. It was observed that PH of the solvent reduced as there was an increase in the number of substitutions of the dopants. Consequently, less NaOH is needed to get to the appropriate PH values and the shape of the platelets undergoes alteration to the sphere form.

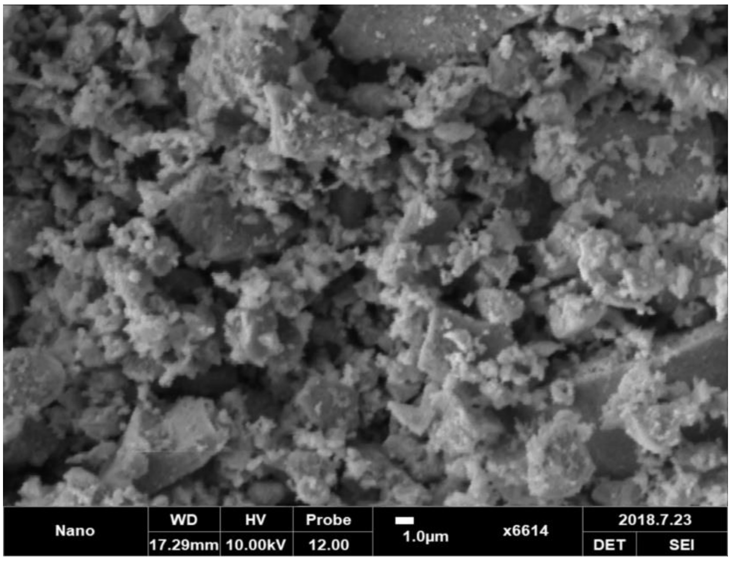

Figure 4.14: SEM Micrograph of Ba$_2$NiCoNd$_x$Fe$_{28-x}$O$_{46}$ at X=0.00 at T=950˚C

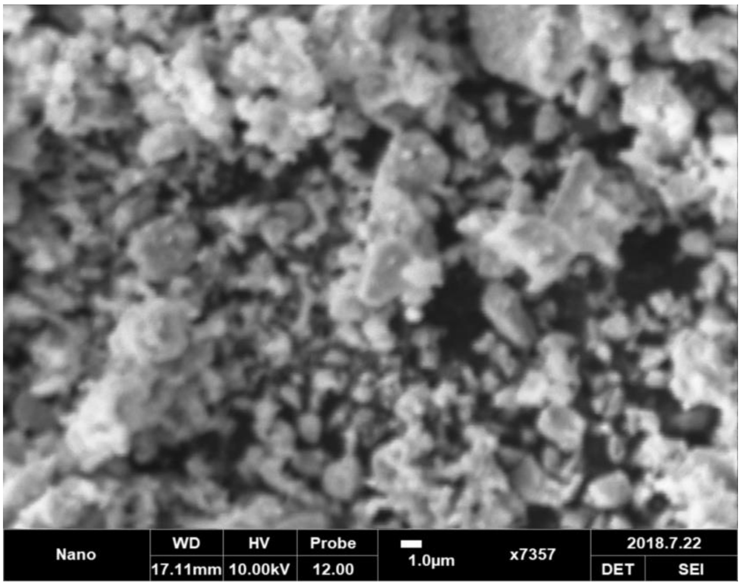

Figure 4.15: SEM Micrograph of Ba$_2$NiCoNd$_x$Fe$_{28-x}$O$_{46}$ at X=0.04 at T=950 ˚C

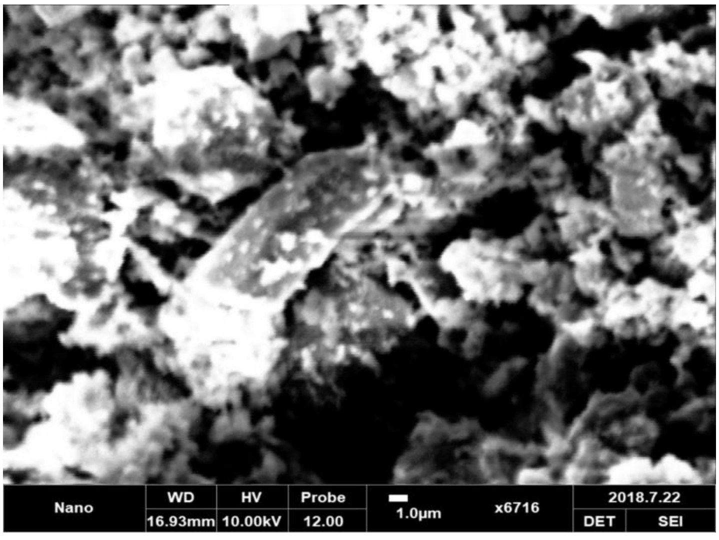

Figure 4.16: SEM Micrograph of Ba$_2$NiCoNd$_x$Fe$_{28-x}$O$_{46}$ at X=0.12 at T=950 ˚C

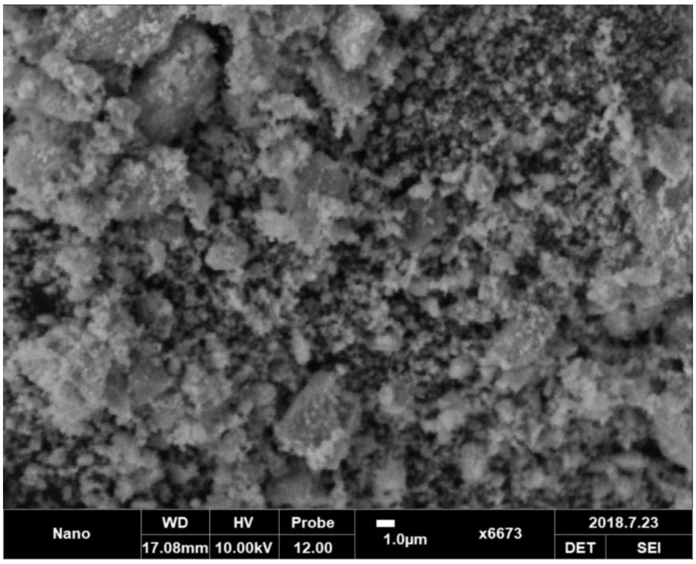

Figure 4.17: SEM Micrograph of Ba$_2$NiCoNd$_x$Fe$_{28-x}$O$_{46}$ at X=0.20 at T=950 ˚C

CONCLUSION

The state of application Nanoferrites has received much attention because of its many practical applications in medicine, farming, the world of modern technology, engineering, and research. These properties can be tuned to include electrical, magnetic, dielectric, microwave, and electromagnetic properties using different synthesis techniques and by use of rare-earth metal in substitution. Of the various methods of preparation, the co-precipitation one is the simplest and the most effective. In this study, Neodymium-substituted X-type hexagonal ferrites with the chemical composition Ba$_2$NiCoNd$_x$Fe$_{28-x}$O$_{46}$ (where x = 0.00 to 0.20) were synthesized via the co-precipitation method. The hexagonal ferrites have a high saturation magnetization and magnetic permeability as well as a broad scope of application in electromagnetic materials and industrial equipment, militancy technology, medical industry and communication devices. The synthesized samples were characterized using X-ray diffraction (XRD), scanning electron microscopy (SEM), and Fourier-transform infrared spectroscopy (FTIR) to analyze their structural, morphological, and magnetic properties. The findings proved that the increase in Neodymium doping concentrations caused the expansion of the lattice constants which affected the magnetic nature of the material namely, the coercivity, permeability, saturation magnetizing and retainability. The results show the possibility of Nd-substituted hexagonal ferrites demanding advanced technology research, which could be used in the further development of the materials in the future.

Competing Interests

There are no conflicts of interest exist among authors of this research paper.

ACKNOWLEDGEMENTS

Authors thanks Dr. Muhammad Shahzad Shifa, Associate Professor PhD Physics (Computer Vision), Post-Doc (Nano ferrites Synthesis & Texture Analysis) Department of Physics, The Islamia University of Bahawalpur providing instrumentation facility.

Author Contributions

M.A.A, H.U, K.K and M.T wrote the main manuscript Draft, writing, M.S.S supervision, M.S.R, M.S.S, G.H and J.M studied Data validation and Editing, Reviewing. All authors reviewed the manuscript outline.

Funding: No external fundings.

Data Availability

No data sets were generated or analysed during the current study.

REFERENCES

- Aboud, M., Ahmad, I., Arshad, S., Liaqat, S., Gilani, Z. A., Nadeem, Q., & Shakir, I.(2017). The Effect of Rare Earth Dy^{+3} Ions on Structural, Dielectric and Electricalbehavior of Ni$_{0.4}$Co$_{0.6}$dy$_y$Fe$_{2-y}$O$_4$ Nano-Ferrites Synthesized by Wet Chemical Approach, Digest Journal of Nanomaterials and Biostructures, 12 (2017), 159-168.
- Ganure, K. A., Dhale, L. A., Katkar, V. T., & Lohar, K. S. (2017). Synthesis and Characterization of Lanthanum-doped Ni-Co-Zn Spinel Ferrites Nanoparticles via Normal Micro-Emulsion Method. *International Journal of Nanotechnology and Applications*, *11*(2), 189-195.
- Gilani, Z., Anjum, M., Shifa, S., Khan, H. U. H., AsgharA, J. U., Usmani, M. & Warsi, M. (2017). Morphological and Magnetic Behavior of Neodymium Doped LiNi$_{0.5}$Fe$_2$O$_3$ Ganure, K. A., Dhale, L. A., Katkar, V. T., & Lohar, K. S. (2017). Synthesis and Nanocrystalline Ferrites Prepared Via Micro-Emulsion Technique. *Dig. J. Nanometer. Biostructures, 12*, 223-228.

- Huang, K., Liu, X., Feng, S., Zhang, Z., Yu, J., Niu, X., ...& Huang, X. (2015). Structural and magnetic properties of Ca-substituted barium W-type hexagonal hexaferrites. *Journal of Magnetism and Magnetic Materials*, *379*, 16-21.
- Kamishima, K., Tajima, R., Watanabe, K., Kakizaki, K., Fujimori, A., Sakai, M., & Abe, H. (2015).Crystallographic and magnetic properties of Cu_2 U-type hexaferrite. *Journal of Magnetism and Magnetic Materials*, *375*, 54-60.
- Malik, H., Khan, M. A., Hussain, A., Warsi, M. F., Mahmood, A., & Ramay, S. M. (2018). Structural, spectral, thermal and dielectric properties of Nd-Ni co-doped Sr-Ba-Cu hexagonal ferrites synthesized via sol-gel auto-combustion route. *Ceramics International*, *44*(1), 605-612.
- Mazumdar, S. C., & Hossain, A. A. (2012).Synthesis and Magnetic Properties of $Ba_2Ni_{2-x}Zn_xFe_{12}O_{22}$. *World Journal of Condensed Matter Physics*, *2*(04), 181.
- Pawar, R. A., Desai, S. S., Tamboli, Q. Y., Shirsath, S. E., & Patange, S. M. (2015).Ce $^{3+}$ incorporated structural and magnetic properties of M type barium hexaferrites. *Journal of Magnetism and Magnetic Materials*, *378*, 59-63.
- Şabikoğlu, B., Reddy, Y. A. K. & Reddy, P. S. (2014).The effect of neodymium substitution on the structural and magnetic properties of nickel ferrite *Journal of Photochemistry and Photobiology B: Biology,* 146, 1–9.
- Sadiq, I., Ali, I., Rebrov, E. V., Naseem, S., Ashiq, M. N., &Rana, M. U. (2014). Influence of Nd-Co substitution on structural, electrical, and dielectric properties of x-type hexagonal nanoferrites. *Journal of materials engineering and performance*, *23*(2), 622-627.
- Seifert, D., Töpfer, J., Langenhorst, F., Le Breton, J. M., Chiron, H., & Lechevallier, L. (2009).Synthesis and magnetic properties of La-substituted M-type Sr hexaferrites. *Journal of Magnetism and Magnetic Materials*, *321*(24), 4045-4051.
- Singh, A., Narang, S. B., Singh, K., Pandey, O. P., & Kotnala, R. K. (2010). Electrical and magnetic properties of rare earth substituted strontium hexaferrites. *Journal of ceramic processing research*, *11*(2), 241-249.
- Töpfer, J., Seifert, D., Le Breton, J. M., Langenhorst, F., Chlan, V., Kouřil, K., & Štěpánková, H. (2015). Hexagonal ferrites of X-, W-, and M-type in the system Sr–Fe–O: A Comparative Study, Journal of Solid State Chemistry 226(2015) 133-141.
- Xu, J., Ji, G., Zou, H., Zhou, Y., & Gan, S. (2011). Structural, dielectric and magnetic properties of Nd-doped Co_2 Z-type hexaferrites. *Journal of Alloys and Compounds*, *509*(11), 4290-4294.
- Singh, S., Singh, A., Yadav, B. C., & Dwivedi, P. K. (2013). Fabrication of nanobeads structured perovskite type neodymium iron oxide film: its structural, optical, electrical and LPG sensing investigations. *Sensors and Actuators B: Chemical*, *177*, 730-739.
- Opuchovic, O., Kreiza, G., Senvaitiene, J., Kazlauskas, K., Beganskiene, A., & Kareiva, A. (2015).Sol-gel synthesis, characterization and application of selected sub-microsized lanthanide (Ce, Pr, Nd, Tb) ferrites. *Dyes and Pigments*, *118*, 176-182.
- Mahgoob, A., & Hudeish, A. Y. (2012).Thermal annealing effect on the structural and magnetic properties of barium hexaferrite powders. *American Academic & Scholarly Research Journal*, *4*(5), 1.
- Meaz, T. M., Saafan, S. A., El-Ghazzawy, E. H., Ayad, M. M., & El Nimr, M. K. (2012). Comparative Study of Dielectric Properties of (Ni Zn Ferrite Nanoparticles/Polypyrrole) Composites with different PPy percentages. *Journal of American Science*, *8*(8).
- Jamil, Y., Ahmad, M. R., Hafeez, A., ul Haq, Z., & Amin, N. (2008). Microwave assisted synthesis of fine magnetic manganese ferrite particles using co-precipitation technique. *Pakistan Journal of Agricultural Sciences*, *45*(3), 59-64.
- Farid, M. T., Ahmad, I., Aman, S., Kanwal, M., Murtaza, G., Ali, I., ...& Ishfaq, M. (2015). Structural, electrical and dielectric behavior of $Ni_xCo_{1-x}Nd_yFe_{2-y}O_4$ nano-ferrites synthesized by sol-gel method. *Digest Journal of Nanomaterials and Biostructures*, *10*(1), 265-275.
- Nakano, A., Nakano, J., & Seetharaman, S. (2015). Synthesis of nano-manganese ferrite by an oxalate method and characterization of its magnetic properties. *International Journal of Materials Research*, *106*(12), 1264-1268.
- Agouriane, E., Rabi, B., Essoumhi, A., Razouk, A., Sahlaoui, M., Costa, B. F. O., &Sajieddine, M. (2016).Structural and magnetic properties of $CuFe_2O_4$ ferrite nanoparticles synthesized by co-precipitation. *J. Mater. Environ. Sci*, *7*(11), 4116-4120.
- Sagadevan, S., Chowdhury, Z. Z., & Rafique, R. F. (2018).Preparation and Characterization of Nickel ferrite Nanoparticles via Co-precipitation Method. *Materials Research*, *21*(2).
- Mahmood, S., &Bsoul, I. (2017).Tuning the Magnetic Properties of M-type Hexaferrites. *arXiv preprint arXiv:1707.07243*.
- Mahmood, S. H., Zaqsaw, M. D., Mohsen, O. E., Awadallah, A., Bsoul, I., Awawdeh, M., & Mohaidat, Q. I. (2016).Modification of the magnetic properties of Co2Y hexaferrites by divalent and trivalent metal substitutions.In *Solid State Phenomena* (Vol. 241, pp. 93-125).Trans Tech Publications.
- Elahi, I., Zahira, R., Mehmood, K., Jamil, A., & Amin, N. (2012).Co-precipitation synthesis, physical and magnetic properties of manganese ferrite powder. *African journal of pure and applied chemistry*, *6*(1), 1-5.

- La, P., Lei, W., Wang, X., Wei, Y., & Ma, Y. (2015). Effects of excess $NaClO_4$ on phases, size and magnetic properties of Ni–Zn ferrite powders prepared by combustion synthesis. *Ceramics International*, *41*(8), 9843-9848.
- Grossinger, R., Kupferling, M., Blanco, J. T., Wiesinger, G., Muller, M., Hilscher, G., ...& Harris, I. R. (2003). Rare earth substitutions in M-type ferrites. *IEEE transactions on magnetics*, *39*(5), 2911-2913.
- Mohsen, W., Sadek, M. A., & Elazab, H. A. (2017).Green synthesis of copper oxide nanoparticles in aqueous medium as a potential efficient catalyst for catalysis applications. *International Journal of Applied Engineering Research*, *12*(24), 14927-14930.
- Irfan, S., Ajaz-un-Nabi, M., Jamil, Y., & Amin, N. (2014).Synthesis of $Mn_{1-x}Zn_xFe_2O_4$ ferrite powder by co-precipitation method. In *IOP Conference Series: Materials Science and Engineering* (Vol. 60, No. 1, p. 012048). IOP Publishing.
- Greene, D., Serrano-Garcia, R., Govan, J., & Gun'ko, Y. K. (2014).Synthesis characterization and photocatalytic studies of cobalt ferrite-silica-titania nano composites. *Nanomaterials*, *4*(2), 331-343.
- Mosleh, Z., Kameli, P., Poorbaferani, A., Ranjbar, M., & Salamati, H. (2016). Structural, magnetic and microwave absorption properties of Ce-doped barium hexaferrite. *Journal of Magnetism and Magnetic Materials*, *397*, 101-107.
- Ati, M. A., Khudhair, H., Dabagh, S., Rosnan, R. M., &Ati, A. A. (2014). Synthesis and Characterization of Cobalt doped Nickel-Ferrites Nanocrystalline by Co-precipitation Method. *International Journal of Scientific & Engineering Research*, *9*(9),927-930.
- Sadiq *et al.,*Nanosized Ce-Zn substituted microwave absorber material for X-typeband applications, J. Magn. Magn. Mater. 370 (2014) 25-31.
- Yan, B., Gao, P. Z., Lu, Z. L., Ma, R. X., Rebrov, E. V., Zheng, H. B., & Gao, Y. X. (2015). Effect of Pr^{3+} substitution on the microstructure, specific surface area, magnetic properties and specific heating rate of $Ni_{0.5}Zn_{0.5}PrxFe_{2-x}O_4$ nanoparticles synthesized via sol–gel method. *Journal of Alloys and Compounds*, *639*, 626-634.
- Lodhi, M. Y., Khan, M. A., Akhtar, M. N., Warsi, M. F., Mahmood, A., &Ramay, S. M.(2018). Role of Nd-Ni on structural, spectral and dielectric properties of strontium-bariumbased nano-sized X-type ferrites. *Ceramics International*, *44*(3), 2968-2975.
- Ahmad, M., Grössinger, R., Kriegisch, M., Kubel, F., &Rana, M. U. (2013).Characterization of Sr-substituted W-type hexagonal ferrites synthesized by sol–gel auto combustion method. *Journal of Magnetism and Magnetic Materials*, *332*, 137-145.
- Jiang, X., Li, S., Yu, Z., Harris, V. G., Su, Z., Sun, K., ...& Lan, Z. (2018). Effect of cobalt substitution on magnetic properties of $Ba_4Ni_{2-x}Co_xFe_{36}O_{60}$ hexaferrite. *AIP Advances*, *8*(5), 056218.
- Ahmad, M., Ali, I., Grössinger, R., Kriegisch, M., Kubel, F., &Rana, M. U. (2013).Effects of divalent ions substitution on the microstructure, magnetic and electromagnetic parameters of Co2W hexagonal ferrites synthesized by sol–gel method. *Journal of Alloys and Compounds*, *579*, 57-64.
- Iqbal, M. J., & Khan, R. A. (2009). Enhancement of electrical and dielectric properties of Cr doped $BaZn_2$ W-type hexaferrite for potential applications in high frequency devices. *Journal of Alloys and Compounds*, *478*(1-2), 847-852.
- Rashad, M. M., El-Sayed, H. M., Rasly, M., Sattar, A. A., & Ibrahim, I. A. (2013). Magnetic and dielectric properties of polycrystalline La doped barium Z-type hexaferrite for hyper-frequency applications. *Journal of Materials Science: Materials in Electronics*, *24*(1), 282-289.
- Ahmad, M., Grössinger, R., Kriegisch, M., Kubel, F., & Rana, M. U. (2012). Magnetic and microwave attenuation behavior of Al-substituted Co_2W-type hexaferrites synthesized by sol-gel auto combustion process. *Current Applied Physics*, *12*(6), 1413-1420.
- Kanagesan, S., Hashim, M., Kalaivani, T., Ismail, I., Rahman, N. A., & Hajalilou, A. (2014). Microwave sintering of Ni-Co doped barium strontium hexaferrite synthesized via sol-gel method. *Journal of Chemical and Pharmaceutical Research*, *6*(4), 1210-1215.
- Bhukal, S., Namgyal, T., Mor, S., Bansal, S., & Singhal, S. (2012). Structural, electrical,optical and magnetic properties of chromium substituted Co–Zn nanoferrite $Co_{0.6}Zn_{0.4}Cr_xFe_{2-x}O_4$ ($0\leqslant x\leqslant 1.0$) prepared via sol–gel auto-combustion method. *Journal of Molecular Structure*, *1012*, 162-167.
- Alam, R. S., Moradi, M., Rostami, M., Nikmanesh, H., Moayedi, R., & Bai, Y. (2015).Structural, magnetic and microwave absorption properties of doped Ba-hexaferrite nanoparticles synthesized by co-precipitation method. *Journal of Magnetism and Magnetic Materials*, *381*, 1-9.
- Khan, M. A., Hussain, F., Rashid, M., Mahmood, A., Ramay, S. M., & Majeed, A. (2018). Structural elucidation and magnetic behavior evaluation of Cu-Cr doped BaCo X-type hexagonal ferrites. *Journal of Magnetism and Magnetic Materials*, *452*, 73-79.
- Kagdi, A. R., Solanki, N. P., Carvalho, F. E., Meena, S. S., Bhatt, P., Pullar, R. C., & Jotania, R. B. (2018). Influence of Mg substitution on structural, magnetic and dielectric properties of X-type barium zinc hexaferrites $Ba_2Zn_{2-x}Mg_xFe_{28}O_{46}$. *Journal of Alloys and Compounds*, *741*, 377-391.